Applied Physics A manuscript No.
(will be inserted by the editor)

Compositional and Structural Properties of Pulsed Laser Deposited ZnS:Cr Films

Mohammadreza Nematollahi[1], Xiaodong Yang[1], Eivind Seim[1], Per Erik Vullum[1,2], Randi Holmestad[1], Ursula J. Gibson[1], Turid W. Reenaas[1]

[1] Department of Physics, Norwegian University of Science and Technology, 7491 Trondheim, Norway

[2] SINTEF Materials and Chemistry, Postboks 4760 Sluppen, Trondheim, 7465, Norway

Received: date / Revised version: date

Abstract We present the properties of Cr-doped zinc sulfide (ZnS:Cr) films deposited on Si(100) by pulsed laser deposition (PLD). The films are studied for solar cell application, and to have a high absorption a high Cr content (2.0–5.0 at.%) was intended. It is determined by energy-dispersive X-ray spectroscopy that Cr is relatively uniformely distributed, and Cr increase corresponds to Zn decrease. The results indicate that most Cr atoms substitute Zn sites. Consistently, electron energy loss and X-ray photoelectron spectroscopy (XPS) showed that the films contain mainly Cr^{2+} ions. Structural analysis showed that the films are polycrystalline and textured. The films with ~ 4 % Cr are mainly grown along the hexagonal [001] direction in wurtzite phase. The average lateral grain size decreases with

Correspondence to: nematollahim@gmail.com

increasing Cr content, and at a given Cr content, increases with increasing growth temperature.

Key words Pulsed laser deposition – Cr-doped ZnS – Crystal structure – Transmission electron microscopy

1 Introduction

The optical, electrical, structural and magnetic properties of chromium doped zinc sulphide (ZnS:Cr) have been investigated since the 1970s [1–7]. Recently, ZnS:Cr has been proposed as an intermediate band (IB) material by *ab initio* calculations [8] for use in intermediate band solar cells (IBSCs) [9]. In addition, ZnS:Cr has several potential optoelectronic and spintronic applications: It has been studied as laser material in tunable near- and mid- infrared lasers [10, 11], and can potentially be used for various spintronic applications [12]. ZnS:Cr is also known as a dilute ferromagnetic semiconductor and room temperature ferromagnetism has been demonstrated [13].

There are surprisingly few reports on film growth of Cr-doepd ZnS. In the majority of the previous studies on lasing properties, bulk ZnS:Cr crystals have been prepared. In most cases, a two-stage method has been used: First chemical vapor transport is used to deposit ZnS and afterwards thermal diffusion has been used for the Cr doping. Ichino *et al.* [14] have demonstrated epitaxial growth of $\mathrm{Zn_{1-x}Cr_xS}$ $(x \leq 0.04)$ on GaP by molecular beam epitaxy (MBE). In that work, for $x > 0.015$ a $\mathrm{ZnCr_2S_4}$ phase was detected in addition to cubic/zinc blende

ZnS:Cr. Vlasenko *et al.* [15] have reported on co-evaporation of ZnS and Cr for use in waveguides. Pulsed laser deposition (PLD) of ZnS:Cr films has been reported by Wang *et al.*[16] for application in lasers. Typically, the Cr content in ZnS:Cr as laser materials is less than $4.0\times10^{20}\,\mathrm{cm}^{-3} \simeq 0.8$ at.%. However, for application as IB material high Cr content is desired to have high sub-bandgap absorption. High doping level results in different physical properties, which needs to be studied for the new applications of ZnS:Cr.

ZnS (and also doped ZnS) has two basic structures, zincblende and wurtzite, and a large number of other polytype structures [17]. The difference of various polytype structures is just the stacking and repeating orders of two-dimensional layers along the hexagonal [001] c axis (corresponds to cubic [111] axis). In addition, it has been observed that Cr dopant converts the structure of ZnS crystals from cubic to the complex ordered or disordered polytypical structures along one dimension [18]. However, a complete structure conversion from cubic (3C, ABCABC order) to hexagonal (2H, ABAB order) is not reported as mentioned in Ref. [3]. We have also seen an increase in the degree of hexagonality with increasing Cr content in the ZnS:Cr films, which is addressed in the current article.

In this work, we deposit ZnS:Cr on Si(100) by PLD. ZnS and Si has lattice mismatch of 0.40 % which is very low compared to other substrates like GaAs, GaP, Ge, and Al_2O_3 [19]. But, due to thermal expansion difference and polarity, Si is not an ideal match with ZnS and nor are the other substrates mentioned above. Another challenge to deposition of crystalline doped or un-doped ZnS on Si is reaction of sulfur with Si and formation of a surface layer unfavorable for

ZnS/Si heteroepitaxial growth [20]. Possible solutions to this problem are either passivation of the Si substrate by an arsenic layer [21], or use of PLD and high temperature growth [22]. In the former solution, a thin arsenic layer was remained at the interface of ZnS and Si. In the latter one, a highly ordered film is formed from the ZnS species (neutral, or ionized) that are present in the plume and all atomic species are re-evaporate due to high substrate temperature. Despite various challenges mentioned above, we used Si as substrate for several reasons: i) The primary purpose of this work is investigation on ZnS:Cr for use in IBSCs, and Si has a bandgap well-suited for use in a tandem cell in combination with a ZnS-based IBSC [23]. ii) Silicon is an earth abundant material like ZnS. iii) ZnS has been deposited on Si in several works and many challenges are known [19,24]. However, deposition of ZnS:Cr on Si is reported only in a few works [16].

Previously, we reported on MBE and PLD growth of highly doped (2.0–7.5 %) ZnS:Cr films on Si(100) for use in IBSCs [25]. We observed that introducing Cr into ZnS results in Cr related sub-bandgap absorption, but also reduced the grain size for both deposition methods. The sub-bandgap absorption increased with increasing Cr content, and with increasing growth temperature, but did not depend on growth method. In contrast, the crystal structure and grain morphology depended strongly on the growth method, and smoother and highly textured films were obtained by PLD. Therefore, we present here a more detailed analysis of the structural properties of PLD grown films as they showed best potential for use in IBSCs. The scope of the work is materials growth and characterization, while we have reported device properties in Ref. [26].

2 Experimental details

2.1 Growth

A KrF excimer laser (Lambda Physics COMPex Pro 110, λ =248 nm, pulsed duration FWHM of 20 ns) was operated at 5 Hz to ablate a $(\mathrm{ZnS})_{0.94}\mathrm{Cr}_{0.06}$ (ZnSCr) target (99.99 %, Super Conductor Materials, Inc.) for deposition of ZnS:Cr films. The laser beam was imaged onto the target with an incident angle of 45°. The laser spot size on the target, A_s, was $\sim 1 \times 2\,\mathrm{mm}^2$, and for one sample $A_s \sim 0.7 \times 1.7\,\mathrm{mm}^2$. To avoid formation of craters, the targets were scanned, exposing an area of $\sim 10 \times 20\,\mathrm{mm}^2$ to the laser beam. Before each deposition, the targets were polished and pre-ablated by a number of pulses, N_P. The ZnSCr target consisted of Cr particles $(20 - 100\,\mu\mathrm{m})$ embedded in a ZnS:Cr matrix (the Cr content in the matrix was not determined). As demonstrated in Ref. [27], the Cr content in the films could be varied reproducibly, simply by varying the laser fluence ($\phi = 1.0 - 7.8\ \mathrm{J/cm}^2$). For instance, increasing ϕ, resulted in a higher Cr/Zn cation ratio in the depositing flux (plasma plume). ZnS:Cr films with Cr content between ($x = 2.0 - 5.0$ at.%) were deposited on Si(100) substrates. Prior to deposition, the substrates were degreased using ethanol and acetone. In order to remove the native oxide on Si, the substrates were etched in 5 % HF for 3 minutes followed by 3 minutes rinsing in deionized water. Next, the substrates were transferred to the PLD chamber, and heated to $850\,^{\circ}\mathrm{C}$ in the chamber (at base pressure of $\leq 5 \times 10^{-6}\,\mathrm{Pa}$). The substrates were kept at high temperature for 2 minutes and then the temperature was lowered to the temperature used during growth (T_S).

Table 1 Sample list including nominal growth temperature, T_S, and fluence, ϕ, number of laser pulses, N_T, target to substrate distance, d_{TS}, background pressure, P_B, and selected measured film properties; Film thickness, d, growth rate, R, Cr content, x, and the XRD peak width (FWHM), B, and corresponding crystallite size, D. The XRD peak labeling is described in the text. Films are labeled as Ax/T_S, Bx/T_S, and Cx/T_S.

	T_S	ϕ	N_P	N_T	d_{TS}	P_B	d / R	x	B / D
	[°C]	[J/cm^2]	×1000	×1000	[cm]	[Pa]	[nm] / [Å/pulse]	[at.%]	[°] / [nm]
A3.0/500	500	3.9	4	16	7	0.3	250 / 0.16	3.0	0.89/ 10
A2.0/550	550	1.0	7	15	7	0.3	151 / 0.10	2.0	0.28/ 32
A3.0/550	550	2.1	7	15	7	0.3	218 / 0.15	3.0	0.46 / 20
A3.3/550	550	3.2	7	15	7	0.3	290 / 0.20	3.3	0.66 / 14
A4.0/550	550	4.3	7	15	7	0.3	350 / 0.23	4.0	0.70 / 13
A5.0/550[a]	550	7.8	7	15	7	0.3	175 / 0.12	5.0	0.76 / 12
A4.0/600	600	4.3	7	15	7	0.3	245 / 0.16	4.0	0.33 / 28
B2.6/550	550	3.5	12	4	7	0.3	80/ 0.20	2.6	0.69/ 13
C4.4/550	550	4.1	44	24	8	0.1	300/ 0.13	4.5	Not measured

[a] Different laser spot size $A_s \sim 0.7 \times 1.7\,\mathrm{mm}^2$ (for other samples $A_s = 1.0 \times 2.0\,\mathrm{mm}^2$).

The deposited films are listed in Table 1, where the most important growth parameters and some of the resulting film properties are given. The films are labeled A, B and C depending on the deposition parameters: Films labeled Ax/T_S were all deposited using total number of $N_T = 15000$ laser pulses under a background pressure, P_B, of 0.3 Pa Ar, gas flow 22 SCCM and with target to substrate distance, d_{TS}, of 7 cm. x and T_S are the measured Cr content (in at. %) and substrate

temperature (in $^{\circ}$C), respectively. N_T and N_P were different for film A3.0/500, B2.6/550, and C4.4/550 as given in Table.1. The N_P and the fluence affect the Cr content and growth rate for the films, as shown in Ref. [27].

2.2 Characterization

Rutherford backscattering spectroscopy (RBS). RBS measurements were made with 1.6 MeV He^+ ions backscattered into the detector at 165° relative to the incident beam direction. The measurements were carried out using 1 MV tandem accelerator at the Micro- and Nanotechnology Laboratory (MiNaLab) in UiO, Norway. The film compositions were determined by fitting simulated curves to the experimental spectra using the SIMNRA code [28].

X-ray photoelectron spectroscopy (XPS). XPS was obtained using Kratos Axis Ultra. Since Cr 2p photoelectrons and Zn Auger electrons have the same kinetic energy with monochromatic (Al Kα, $h\nu = 1486.6\,\mathrm{eV}$, lowest energy resolution 150 meV) X-ray energy, we used a non-monochromatic radiation (Mg Kα, $h\nu = 1253.6\,\mathrm{eV}$ with approximate energy resolution of 0.6 eV) source for the measurements. All the binding energies (Eb) were corrected for surface charging by Eb equal to 285.0 eV of adventitious C 1s. The XPS analysis was done initially on as-deposited film (not in the same chamber) and then same measurements repeated right after a gentle Ar^+ (0.5 keV) sputtering, where adventitious carbon and surface adsorbed oxides were removed thoroughly. XPS survey scans were performed within 2 min for surface elemental analysis, and Cr 2p core levels were measured

for Eb range 570-605 eV within 50 min. A pure chromium metal reference sample is used to find out the asymmetric lineshape and width of Cr^0.

X-ray diffraction (XRD). XRD is measured using a Bruker AXS D8 Focus equipped with a LynxEye detector and a Cu-radiation source (CuK$\alpha 1, 2$), with wavelength of 1.5406 Å. The average crystallite size in the films is estimated from the XRD peak broadening by use of the Scherrer equation [29]

$$D = \frac{K\lambda}{B\cos\theta}, \tag{1}$$

where D is the crystallite size, or the coherence length of the sample in nanometers, K is the Scherrer constant set to $K = 1$, λ is the wavelength of the X-rays (0.15406 nm), B is the full-width at half maximum (FWHM) value of the peak, and θ is the Bragg angle. It should be noted that D obtained from the XRD analysis can be smaller than the grain size measured by other methods due to presence of defects such as dislocations and stacking faults [30]. Also note that D is the vertical crystallite size, not the lateral or in-plane crystallite size.

Scanning electron microscopy (SEM). A Hitachi S-5500 has been used for the SEM studies .

Transmission electron microscopy (TEM). For the TEM studies a JEOL 2100 TEM equipped with a LaB6 source has been used for low magnification imaging and diffraction work, while a double Cs aberration corrected coldFeg JEOL ARM200F has been used for high resolution imaging, high angle annular dark field (HAADF) scanning TEM (STEM) and energy-dispersive X-ray spectroscopy (EDS). The ARM is equipped with a Centurio silicon drift detector EDS system and a fast dualEELS GIF. Dual EELS and EDS were collected simultane-

ously by several line scans both perpendicular and parallel to the substrate interface in scanning TEM (STEM) mode. One of the EEL spectra included the zero loss peak (to calibrate the energy), the second spectrum included the Cr L2,3 peaks.

Sample preparation. Both plan-view and cross-sectional geometries were studied in the SEM and TEM to obtain more information on crystallography and grain structure in the films. For SEM cross-section images, the films were simply cleaved along the $\langle 110 \rangle$ crystalline planes of the Si substrate. For TEM cross-section and plan-view, foils were prepared by grinding, dimpling, followed by low-energy Ar-ion milling, using a Gatan PIPS as explained in details elsewhere [31]. Liquid N_2 was used to cool the sample during milling. Plan-view samples were made by grinding and polishing from the substrate side, and Si has been completely removed.

Film thickness. The film thicknesses were measured by a profilometer (Dektak 150) and also from cross-section SEM images.

3 Results and Discussion

3.1 Growth rate and film thickness

The growth rate, R, and film thickness, d, for the films are listed in Table 1. R and d are in the range 0.10 – 0.23 Å/pulse and 80-350 nm, respectively. It can be seen that R increases as ϕ increases for sample A2.0/550 to A4.0/550. Note that both R and d for A5.0/550 is lower than A4.0/550, despite the higher ϕ used for A5.0/550. The decrease is related to the small laser spot size, A_s, used for A5.0/550. In addition, R decreases with increasing T_S from $550\,^{\circ}\mathrm{C}$ to $600\,^{\circ}\mathrm{C}$ (compare A4.0/550

and A4.0/600). Deposition using $T_S > 600\,^{\circ}\mathrm{C}$ was also attempted, but no film was formed at the growth conditions used here (laser fluence and repetition rate, target-substrate distance, background pressure). This can be due to increased re-evaporation during growth.

To obtain a uniform thickness, d_{TS} was set to 7–8 cm, resulting in a thickness fluctuation within 5 % over a $1\,\mathrm{cm}^2$ sample.

3.2 Film composition

A typical RBS spectrum of one of the films (sample A4.0/550) is presented in Fig. 1. According to the simulation results, the films are close to stoichiometric with [S]/[Zn+Cr] ratio of $(1.00-1.04)\pm0.03$. We did not observe any impurities in the films. The Cr content, x measured by RBS, in each film is listed in Table 1, and we see that for a given T_S, x increases with increasing laser fluence. In addition, increasing T_S from $550\,^{\circ}\mathrm{C}$ to $600\,^{\circ}\mathrm{C}$ results in a higher Cr content in the film. As we reported in Ref. [27], the Cr/Zn ratio in the depositing flux is dependent on the ablation parameters, such as laser fluence, and the target surface morphology. However, we expect that the final Cr content in the ZnS:Cr films to be dependent on T_S. This is due to the high vapour pressure of Zn compared to Cr.

The local variation of the Cr content in the films was studied qualitatively and quantitatively by EDS maps and line-scans, respectively. A HAADF STEM image for cross-section B2.6/550 is shown in Fig. 2(a) and element maps for Zn, S, Cr and O are presented in Figs. 2(b)-(e). As can be seen from the figure, Cr seems relatively uniformly distributed, but with some variations. Also, note the uniform

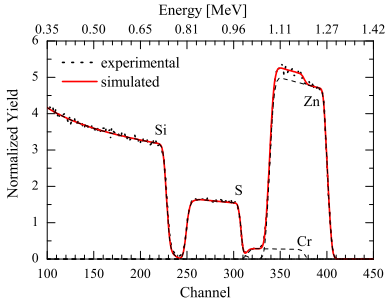

Fig. 1 RBS spectrum of A4.0/550 with 4.0 at.% Cr and 350 nm thickness. The solid line is a simulation, and the dashed lines indicate the signals from individual elements.

Zn and S content across the thin film. We see a monotonic S decrease towards the thin film surface due to the decrease in TEM sample thickness. In the Zn map we see the same decrease, but at the surface we probably have a ZnO layer. The oxygen we see in the EDS line-scans are due to thin oxidation layers on top and at the bottom of the thin TEM foils. This oxygen is not an intrinsic property of the film, but a result of the TEM sample preperation. We are not able to prepare the TEM sample under inert atmosphere at all times. Hence, the surface of the TEM foil will be oxidized before the TEM sample is loaded into the TEM.

Typical HAADF STEM images of cross-section C4.4/550 are given in 2(f) and 2(g). EDS line-scans parallel and perpendicular to the film-substrate interface are indicated on the images. For the line-scans Si and O are subtracted from the data, and the sum of Zn, S and Cr fractions are normalized to 100 %. The result of a parallel EDS line-scan for C4.4/550 is presented in Fig. 2(h). It can be seen that the Cr and Zn amounts are varying along the scanned line, while the S content is rather constant. As for the EDS map in Fig. 2(d), we see that the Cr content varies along the line scans. At some locations the Cr content is as high as 11 %,

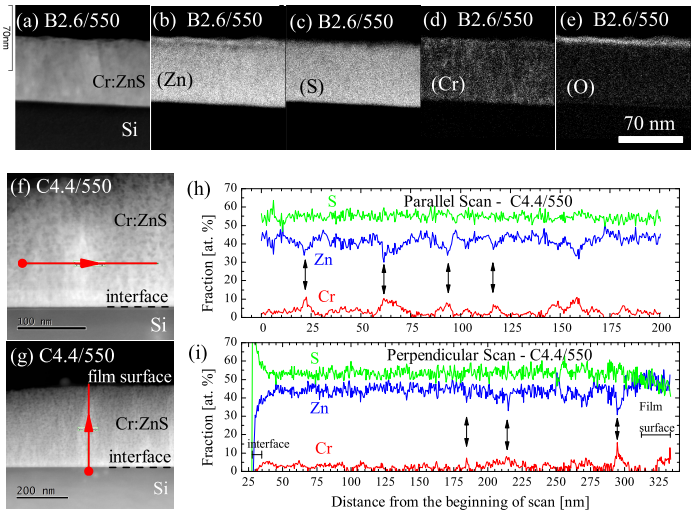

Fig. 2 (a) HAADF STEM image, Qualitative (as a function of raw counts) EDS map for (b) Zn, (c) S, (d) Cr and (e) O of cross-section B2.6/550. HAADF STEM images of cross-section C4.4/550 showing the position of EDS line-scans (f) parallel and (g) perpendicular to the film-substrate interface. Arrows and circles show the direction and the start point of the scans, respectively. (h) Parallel and (i) perpendicular line-scans, showing the fractions of Zn (blue), S (green), and Cr (red). Areas with higher Cr and lower Zn are indicated by vertical flashes.

while in some locations no Cr can be detected. The fact that the locations where the Cr content increases coincides with a decrease in Zn content, suggests that Cr substitutes Zn sites within the film, but with local concentration variations. The result for the perpendicular EDS line-scan for C4.4/550 is shown in Fig. 2(i). In this scan both Cr and Zn vary less compared to the parallel line scan. In addition, the first 3–4 nm of the film close to the interface contains more S than higher up in the film. The film surface, in contrast, contains less S in comparison to most other parts of the film. Note that the S:Zn ratio is significantly larger than 1 in the line

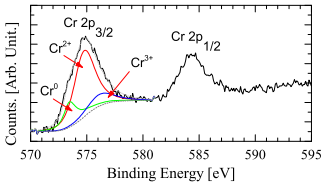

Fig. 3 XPS of Cr 2p for (Ar^+ sputtered) A3.0/500 film. Acquired data (solid line), background (dashed line), fitted line (dotted line), and deconvoluted peaks (solid lines) for Cr^0 (green), Cr^{2+} (red) and Cr^{3+} (blue).

scans. This ratio does not reflect the real chemical composition, but is primarily due to a slightly wrong theoretical k-factor in the Cliff-Lorimer equation that is the basis for the quantifications. Also note that the reduced S on the surface in Fig. 2(i) is caused by transformation of ZnS to ZnO. The Zn and Cr values are incorrect near the surface, since oxygen is not included in the line scans.

3.3 Cr valence state

XPS was mainly performed to determine Cr valence states in the films. From the survey scans, no impurity element was observed in the films, as expected and also confirmed by RBS. Typical Cr 2p peaks are shown in Fig. 3 for Ar sputtered A3.0/500 film. All species of Cr 2p core level are consisted of two peaks, namely Cr $2p_{3/2}$ and Cr $2p_{1/2}$ with spin-orbit splitting of $\sim 9.2\,\mathrm{eV}$ [32].

Before the peak fitting, Shirley background (dashed line) is subtracted from the spectrum. Peak fitting is performed only for Cr $2p_{3/2}$ (solid lines) as it is done similarly by Li and Hu. [33]. Instead of comparing the actual binding energy values in literature, the binding energy differences are used to identify chemical states

of Cr. Metallic Cr core level has the lowest binding energy, so the shoulder at $\sim 573.4\,\mathrm{eV}$ is related to presence of Cr^0. The biding energy of Cr^{2+} is 1.3 eV [32,34] higher than that of Cr^0 ($\Delta[\mathrm{Cr}^{2+} - \mathrm{Cr}^0] = 1.3\,\mathrm{eV}$). To have a good fitting a third peak related to Cr^{3+} is added ($\Delta[\mathrm{Cr}^{3+} - \mathrm{Cr}^0] = 2.7\,\mathrm{eV}$) [32]. For Cr^0, asymmetric lineshape and width of a pure chromium metal reference sample is used. For Cr^{2+}, a mixed Gaussian-Lorentzian product lineshape is used. Multiplet splitting has been observed for Cr^{3+} core level electrons [35], but we could only see an asymmetric broadening[36]. The line broadening is partially due to the utilization of the non-monochromatic X-ray source.

According to XPS results, Cr^{2+} is the major component in the deposited films. In addition, XPS shows that an amount of Cr^0 and Cr^{3+} is present in the films. No signal can be attributed to Cr^{4+}, Cr^{5+}, or Cr^{6+}. The presence of Cr^{+} species between $\mathrm{Cr}^0$and Cr^{2+} peaks cannot be excluded. XPS investigation on other films deposited under similar growth condition shows small differences, but the main features are similar. It is also confirmed by EELS that the valence state of Cr in C4.4/550 is II, Cr^{2+} [37].

The presence of Cr^{2+} is known to be present in ZnS:Cr films with lower Cr content and Cr^{2+} substitute Zn^{2+} sites [5], while other Cr species like Cr^{3+} (Cr^{+} if present) might be at interstitial sites. It has been known that Cr states are located within ZnS bandgap depending on the Cr site and its valence states [5].

3.4 Structural properties

First, we study the XRD patterns of the films presented in Fig.4. No peaks related to metallic Cr, chromium sulfide phases, or $ZnCr_2S_4$ were observed in the films. According to the XRD results, all of the films have one peak at $2\theta \sim 28.6\,^\circ$ which can be assigned to both (111) oriented zincblende (Zb) and (002) oriented wurtzite (Wz). This is because the two Zb(111) and Wz(002) diffraction peaks from Zb and Wz phases are almost at the same angle. So with the relatively broad XRD peaks, it is not possible to resolve the two phases. Thus, we label the XRD peak at $2\theta \sim 28.6^\circ$ 'ZW'. This means that $\theta-2\theta$ XRD scans cannot determine whether the films are exclusively Zb or Wz, or a combination of both phases. More elaborate techniques like XRD φ-scan or TEM are required to determine the correct phase. However, the very weak, unique Wz(100) peak is observed for two films; A3.3/550 and A4.0/550, which is a clear sign for presence of Wz phase in those films, see Figs. 4(c) and 4(d).

The FWHMs of the ZW peak and the corresponding crystallite size calculated by Eq. (1), are listed in Table 1 for series A and B. As can be seen from the Table 1, the average crystallite size associated with the ZW peak decreases with increasing Cr content. Furthermore, at a given Cr content, the crystallite size increases with increasing T_S, which can be seen by comparing the results for A4.0/550 and A4.0/600.

Next, we study the top-view and cross-sectional SEM images of selected films, shown in the left and the right panels of Fig. 5, respectively. From the left panels of Fig. 5(a)-(c), we see that the films are not epitaxial and consist of grains with clear

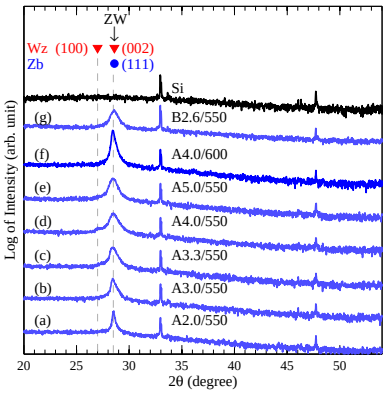

Fig. 4 XRD patterns of ZnS:Cr films. Films are labeled as Ax/T_S, where x is Cr content and T_S is growth temperature. The XRD pattern for a Si(100) substrate is shown in top, and Zb(111) and Wz related peaks are indicated by circles (blue) and triangles (red).

grain boundaries. It can be seen in Figs. 5(a) and 5(b) that the in-plane grain size (lateral grain size, normal to the growth direction) of the ZnS:Cr films decreases with increasing Cr content: A2.0/550 with 2.0 % Cr has grains with in-plane grain size of up to 100 nm, and A4.0/550 with 4.0 % Cr has many grains with in-plane grain size in the range of only a few nm. (Note that the thickness of A4.0/550 is more than twice the thickness of A2.0/550.) In Ref. [25], we have presented a discussion on how an increase in the Cr content in ZnS:Cr films results in smaller grain size. We believe that the Cr atoms act as nucleation centers in the growth process. So, a higher Cr content is accompanied by a higher number of nucleation centers. So, the higher density of smaller grains in the films with more Cr is understood. By comparing A4.0/550 in Fig.5(b) and A4.0/600 in Fig.5(c) we see that the in-plane grain size is larger for higher T_S at a given Cr content. The grains in A4.0/600 seem to have coalesced into larger grains due to the high T_S.

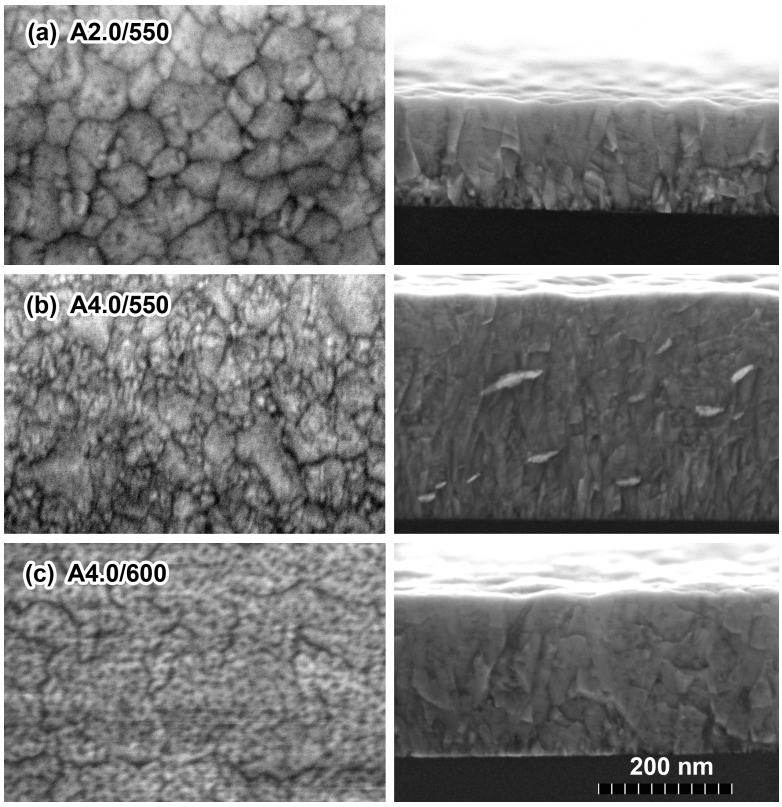

Fig. 5 Top-view (left) and cross-section (right) SEM images of (a) A2.0/550 , (b) A4.0/550, and (c) A4.0/600. The scale bar for all images is 200 nm.

Cross-sectional SEM images of A2.0/550 and A4.0/550 are shown in the right panel of Fig. 5(a) and 5(b), respectively. It can be seen for both films that the in-plane grain size is very small at the film/substrate interface, and that the grain widths increase gradually with film thickness. However, the grain size in the film grown at $600\,^{\circ}\mathrm{C}$ appears more uniform.

The structural properties are investigated in more details by TEM. A bright field (BF) image and corresponding diffraction pattern for cross-section C4.4/550 are shown in Figs. 6(a) and 6(b), respectively. Evidence of Van der Drift growth

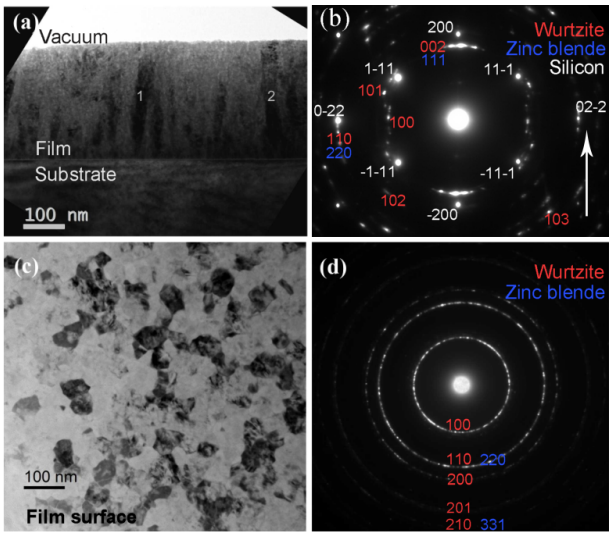

Fig. 6 (a) BF image of cross-section C4.4/550, grains annotated as 1 and 2 have a neeedle-like structure at the interface and expands as the film grows. (b) Corresponding diffraction pattern of cross-section C4.4/550.(c) BF image of plan-view A4.0/600, showing that the grains are in a veriety of shapes, but some grains are faceted. (d) Corresponding diffraction pattern of plan-view A4.0/600. Si substrate is compeletly removed from A4.0/600 during substrate preparation.

can be seen close to the substrate interface, as the grains are initially small, then increase in width through the film [38]. Two of the grains depicting such feature are labeled as 1 and 2 in Fig. 6(a). The corresponding diffraction pattern is presented in Fig. 6(b). It is estimated that about 30 grains contribute to the diffraction pattern. Note that the strong spots are from the Si-substrate, i.e. reflections of [110] zone axis in Si. The diffraction pattern reveals a polycrystalline film with a texture along the growth direction, shown by an arrow on the figure. This shows that the film has

a preference to grow along the cubic [111] in Zb or the hexagonal [001] direction in Wz, as was also seen in the XRD data.

The PLD sample prepared to be studied in plan-view gives a different perspective on the shape of the grains. Plan-view A4.0/660 is presented in Fig. 6(c), showing the grain structure close to the film surface. The grains have an irregular shape with size ranging between 14 and 72 nm, and an average grain size of 38.2 ± 1.6 nm. Note that some of the grains have very defined edges which have facets, and this is another feature of Van der Drift growth [38]. The corresponding diffraction pattern of plan-view A4.0/600 is shown in Fig. 6(d), where ~ 60 grains contribute to the pattern. Note that the Si substrate has been completely removed from A4.0/600 during sample preparation and there is no diffraction spots related to Si in the diffraction pattern. The result shows that the grains have random in-plane orientations, but not all rings can be seen due to the texture.

To study the presented diffraction patterns (Fig. 6), 1-dimensional (1-D) intensity profiles are made by circular integration of the intensities. The concentrically integrated results were then calibrated to match the d-values from the XRD. With such profiles it is easier to read which d-values are present in the diffractograms. In Fig. 7(a) a summary of d_{hkl} values associated with cubic Si, ZnS in the Zb and Wz phases are given. 1-D intensity profiles of C4.4/550 and A4.0/600 are presented in Figs. 7(b) and 7(c) respectively. To make the figure more readable, the main peaks in Figs. 7(b) and 7(c) are indicated by vertical lines. Note that the vertical lines and d_{hkl} values associated with Si, and Zb and Wz phases have variations of $\sim \pm 0.04$ Å. One reason to this is the uncertainties related to calculation

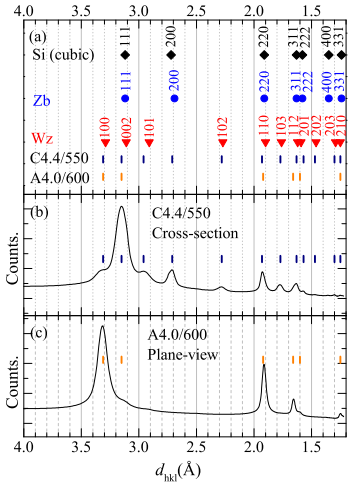

Fig. 7 (a) d_{hkl} values associated with cubic Si (black) and ZnS in the zincblende (Zb, blue) and wurtzite (Wz, red) phases. Vertical dashed lines in navy and orange denotes the peaks in (b) and (c) panels respecively. (b) and (c) One dimensional intensity profiles generated by rotationally averaging diffraction images from cross-sectional C4.4/550, and plan-view A4.0/600 respectively. In c) the Si substrate is compeletly removed from A4.0/600 during substrate preparation.

of 1-D intensity profiles, for instance the central pixel in the direct beam is chosen visually.

According to the 1-D intensity profile of cross-section C4.4/550 (Fig. 7(b)), the main peak at $d = 3.15$ Å attributes to Wz(002)/Zb(111). As mentioned, the same crystalline orientation, labeled ZW, is the main peak in the XRD pattern of all films. In addition, the peak at $d = 3.31$ Å attributes to Wz(100), which is a unique Wz reflection. Wz(100) is also present in the XRD pattern of films with high Cr content (> 0.3 at.%). Note that several other peaks are present in the 1-D intensity profile of cross-section C4.4/550, which are not observed in the

XRD result. Like Wz(100), some of these peaks are also uniquely Wz diffraction, namely Wz(101), Wz(102), Wz(103), W(201), and Wz(203). Therefore, presence of the Wz phase in sample C4.4/550 is proved, while presence of the Zb phase cannot still be excluded.

The main peak in the 1-D intensity profile of plan-view A4.0/600 (Fig. 7(c)) is at $d = 3.32$ Å, which is related to Wz(100) crystalline orientation. The second highest intensity peak at $d = 1.91$ Å can be attributed to Wz(110) and Zb(220). Similar to Wz(002) and Zb(111), the diffracted intensity related to Wz(110) and Zb(220) are almost at the same angle and the reflections cannot be distinguished. Also, note that the number of peaks in the 1-D intensity profile of plan-view A4.0/600 is less than the number of peaks seen in the 1-D intensity profile of cross-section C4.4/550. Therefore, A4.0/600 has a strong texture and since the Wz(100) reflection is very strong, we conclude that the film is close to a pure Wz phase.

High resolution TEM (HRTEM) images for cross-section C4.4/550 and plan-view A4.0/600 are presented in Figs. 8(a) and 8(b), respectively. The insets show Fast Fourier transforms (FFTs) of the middle grain in the corresponding images. The grain shown in Fig. 8(a) has the Wz crystal structure. The lattice spacings and the symmetry are unique for the [100]/[010] orientation of the Wz. The largest lattice spacing corresponds to the distance between the (001) planes (i.e. equal to the length of the c-axis of the Wz unit cell). The (001) reflections are normally absent, but can be seen in the present orientation due to multiple Bragg scattering in TEM. Hence, it can be concluded that this specific grain has the Wz structure. In

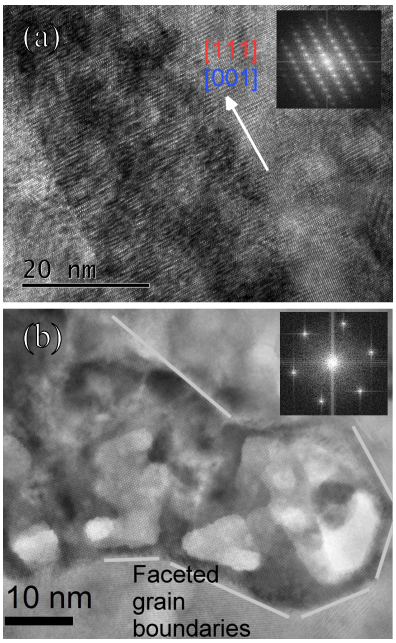

Fig. 8 (a) HRTEM image of a grain in C4.4/550 (cross-sectional). The arrow shows the growth direction of the film, and the inset is a FFT. (b) HRTEM image of a grain in A4.0/600 (plan-view) showing a 6-fold symmetry in the FFT of the central grain. The grain is either a Zb grain seen in the [111] projection or a Wz grain in the [001] projection. The grain shows straight grain boundaries (gray lines) which indicate that it is faceted.

Fig. 8(b) we see a 6-fold symmetry. Both the [001] orientation in Wz and the [111] Zb orientation show this symmetry. However, the lattice spacings are different for the two possibilities. Hence by measuring the distance between the planes in the high resolution image one can conclude about the specific structure for the shown grain. The lattice spacing is $\sim$ 3.33 Å, and this is equal to Wz(100) of the Wz structure. The conclusion that is drawn from Fig. 8 is in agreement with the earlier findings from the diffraction pattern (see Fig. 7(c)).

In the 1-D intensity profile of plan-view A4.0/600 shown in Fig. 7(c), the peak at $d = 3.12$ Å is very weak. This peak corresponds to Zb(111)/Wz(002), labeled ZW in Fig.4. In contrast, the same crystal orientation have a strong peak in the XRD result (see Fig.4(f)). The reason is that top-view orientation in TEM gives Bragg reflections from planes with plane normals parallel to the Si-ZnS interface. In contrast, Bragg reflections in XRD originate from planes with normals along the film growth direction. As a result, the diffractions caused by the planes parallel to the Si-ZnS interface are absent in the electron diffraction pattern. The small intensity of the peak at $d = 3.12$ Å is then related to a small number of grains that have their Wz(002) planes perpendicular to the film surface.

The preliminary results for the crystal structure of the ZnS:Cr thin films are as follows: As mentioned in the introduction, it has been observed that the degree of hexagonality of ZnS:Cr increases with increasing Cr content. In the current study, from the XRD results, it is determined that films with Cr content above ~ 3 % have the unique Wz crystalline planes Wz(100). From the TEM results we found that the phase of ZnS:Cr films with ~ 4.0 % Cr are mainly Wz. Inconsiderable amount of Zb phase could not be ruled out in the highly doped ZnS:Cr films. In general, the growth conditions and parameters may affect the ratio of Wz to Zb in the films. A more systematic TEM study is therefore needed, but this is outside the scope of this work.

4 Conclusion

ZnS:Cr films were deposited by pulsed laser deposition and composition and structural properties were studied by various techniques. The findings of this study is useful for the future investigation of ZnS:Cr for use as an IB material in IBSCs. The Cr content was determined by RBS to be within 2.0–5.0 at.%. In addition, RBS showed that films are stoichiometric, but some of the films were slightly sulfur rich. This study showed that it is possible to achieve a relatively uniform distribution of Cr in ZnS:Cr with sufficiently high Cr content required for a high optical absorption [25]. It was also found that Cr content increase corresponds to Zn content decrease, which suggests that Cr substitutes Zn sites. This is consistent with XPS and EELS results, where it was determined that Cr^{2+} is the major Cr valence state in our ZnS:Cr films. This is in agreement with literature which states that Cr^{2+} substitutes Zn^{2+} sites in ZnS:Cr with much lower Cr content (0.8 at.%). A careful deconvolution of Cr 2p core level suggests that Cr^{0} and Cr^{3+} valence states are also present.

XRD was primarily used for many of the films to determine crystal structure. The results showed that all films are polycrystalline, but highly textured along either the cubic [111] in zincblende or the hexagonal [001] direction in wurtzite phase. Further clarification of the structure was done by TEM studies for some films. According to the TEM results, the main phase of the films with ~ 4 % Cr is wurtzite. Therefore, the wurtzite phase can easily be achieved by doping ZnS with Cr. The average grain size was studied qualitatively using top-view and cross-sectional SEM micrographs, and from TEM results for two films. It was

found that the average lateral grain size decreases with increasing Cr content and at a given Cr content, increases with increasing growth temperature. Similar trend was also observed for crystallite size from the line broadening of XRD peaks. The crystallite size found by XRD $(\sim 10 - 28\,\mathrm{nm})$ was prominently lower than the grain size found by SEM and TEM cross-sections, which is considered to be due to presence of defects in the films.

5 Acknowledgement

This work is done in part within the Norwegian Center for Solar Cell Technology, a Center for Environment-friendly Energy Research co-sponsored by the Norwegian Research Council and research and industry in Norway (project number 193829). The authors also acknowledge the Research Council of Norway for financial support via the Nano2021 program (project number 203503).

References

1. H. Nelkowski and G. Grebe, "IR-luminescence of ZnS:Cr," *J. Lumin.*, vol. 1-2, no. 0, pp. 88–93, 1970.
2. M. Godlewski and M. Kaminska, "The chromium impurity photogeneration transitions in ZnS, ZnSe and ZnTe," *J. Phys. C Solid State*, vol. 13, no. 35, pp. 6537–6546, 1980.
3. G. Goetz and H. J. Schulz, "Influence of the impurity concentration on the microstructure of compound semiconductors - the example of ZnS:Cr optical spectra," *Solid State Commun.*, vol. 84, no. 5, pp. 523–525, 1992.

4. G. Goetz, H. Zimmermann, and H.-J. Schulz, "Jahn-Teller interaction at Cr^{2+}(d 4) centres in tetrahedrally coordinated II-VI lattices studied by optical spectroscopy," *Z. Phys. B Con. Mat.*, vol. 91, no. 4, pp. 429–436, 1993.
5. N. A. Vlasenko, P. F. Oleksenko, Z. L. Denisova, M. O. Mukhlyo, and L. I. Veligura, "Cr-related energy levels and mechanism of Cr^{2+} ion photorecharge in ZnS:Cr," *Phys. Status Solidi B*, vol. 245, no. 11, pp. 2550–2557, 2008.
6. X. Zeng, J. Zhang, and F. Huang, "Optical and magnetic properties of Cr-doped ZnS nanocrystallites," *J. Appl. Phys.*, vol. 111, no. 12, pp. 123525–7, 2012.
7. T. Konak, M. Tekavec, V. V. Fedorov, and S. B. Mirov, "Electrical, spectroscopic, and laser characterization of γ-irradiated transition metal doped II-VI semiconductors," *Opt. Mater. Express*, vol. 3, pp. 777–786, Jun 2013.
8. C. Tablero, "Correlation effects and electronic properties of Cr-substituted SZn with an intermediate band," *J. Chem. Phys.*, vol. 123, no. 11, pp. 114709–7, 2005.
9. A. Luque and A. Martí, "Increasing the efficiency of ideal solar cells by photon induced transitions at intermediate levels," *Phys. Rev. Lett.*, vol. 78, no. 26, pp. 5014–5017, 1997.
10. S. B. Mirov, V. V. Fedorov, I. S. Moskalev, and D. V. Martyshkin, "Recent progress in transition-metal-doped II−VI mid-IR lasers," *IEEE J. Sel. Top. Quant.*, vol. 13, no. 3, pp. 810–822, 2007.
11. N. Vlasenko, P. Oleksenko, M. Mukhlyo, Z. Denisova, and L. Veligura, "ZnS:Cr and ZnSe:Cr thin-film waveguide structures as electrically pumped laser media with an impact excitation mechanism," *Annalen der Physik*, vol. 525, no. 12, pp. 889–905, 2013. cited By 0.
12. D. Amaranatha Reddy, G. Murali, R. P. Vijayalakshmi, and B. K. Reddy, "Room-temperature ferromagnetism in EDTA capped Cr-doped ZnS nanoparticles," *Appl. Phys. A*, vol. 105, no. 1, pp. 119–124, 2011.

13. Z. Zhang, J. Li, J. Jian, R. Wu, Y. Sun, S. Wang, Y. Ren, and J. Li, "Preparation of Cr-doped ZnS nanosheets with room temperature ferromagnetism via a solvothermal route," *J. Cryst. Growth*, vol. 372, pp. 39–42, 2013.

14. K. Ichino, Y. Morimoto, and H. Kobayashi, "Molecular beam epitaxy and structural properties of ZnCrS," *Phys. Status Solidi C*, vol. 3, no. 4, pp. 776–779, 2006.

15. N. A. Vlasenko, P. F. Oleksenko, M. A. Mukhlyo, and L. I. Veligura, "Changes induced in a ZnS:Cr-based electroluminescent waveguide structure by intrinsic near-infrared laser radiation," *Semiconductors*, vol. 47, no. 8, pp. 1116–1122, 2013.

16. S. Wang, S. B. Mirov, V. V. Fedorov, and R. P. Camata, "Synthesis and spectroscopic properties of Cr-doped ZnS crystalline thin films," *Proc. SPIE*, vol. 5332, pp. 13–20, 2004.

17. H. Kuwamoto, "Origin of polytypism in the ZnS structure," *J. Mater. Sci. Lett.*, vol. 4, no. 8, pp. 940–942, 1985.

18. J. Gosk and M. J. Kozielski, "Cr doping influence in ZnS single crystals on the complex disordered polytypical structure," *Cryst. Res. Technol.*, vol. 25, no. 4, pp. 415–419, 1990.

19. Z.-J. Xin, R. J. Peaty, H. N. Rutt, and R. W. Eason, "Epitaxial growth of high-quality ZnS films on sapphire and silicon by pulsed laser deposition," *Semicond. Sci. Technol.*, vol. 14, no. 8, pp. 695–698, 1999.

20. L. T. Romano, R. D. Bringans, X. Zhou, and W. P. Kirk, "Interface structure of ZnS/Si(001) and comparison with ZnSe/Si(001) and GaAs/Si(001)," *Phys. Rev. B*, vol. 52, pp. 11201–11205, Oct 1995.

21. X. Zhou, S. Jiang, and W. P. Kirk, "Epitaxial growth of ZnS on bare and arsenic-passivated vicinal Si(100) surfaces," *J. Appl. Phys.*, vol. 82, no. 5, pp. 2251–2262, 1997.

22. Y. Z. Yoo, Y. Osaka, T. Fukumura, Z. Jin, M. Kawasaki, H. Koinuma, T. Chikyow, P. Ahmet, A. Setoguchi, and S. F. Chichibu, "High temperature growth of ZnS films on bare si and transformation of ZnS to ZnO by thermal oxidation," *Appl. Phys. Lett.*, vol. 78, no. 5, pp. 616–618, 2001.
23. C. Linge, "Modeling of the intermediate band tandem solar cell," Master's thesis, Norwegian University of Science and Technology, 2011.
24. I. P. McClean and C. B. Thomas, "Photoluminescence study of MBE-grown films on ZnS," *Semicond. Sci. Tech.*, vol. 7, no. 11, pp. 1394–1399, 1992.
25. M. Nematollahi, X. Yang, L. M. S. Aas, Z. Ghadyani, M. Kildemo, U. J. Gibson, and T. W. Reenaas, "Molecular beam and pulsed laser deposition of ZnS:Cr for intermediate band solar cells." *Sol. Energ. Mat, Sol. C.*, vol. 141, pp. 322–330, 2015.
26. X. Yang, M. Nematollahi, U. Gibson, and T. Reenaas, "Cr-doped ZnS for intermediate band solar cells," in *Photovoltaic Specialists Conference (PVSC), 2013 IEEE 39th*, pp. 2494–2497, June 2013.
27. M. Nematollahi, X. Yang, U. Gibson, and T. W. Reenaas, "Pulsed laser ablation and deposition of ZnS:Cr." *Thin Solid Films*, vol. 590, pp. 28–32, 2015.
28. SIMNRA (Max-Planck-Institut für Plasmaphysik, 2014).
29. J. I. Langford and A. J. C. Wilson, "Scherrer after sixty years: A survey and some new results in the determination of crystallite size," *J. Appl. Crystallogr.*, vol. 11, pp. 102–113, Apr 1978.
30. A. Boulle, C. Legrand, R. Guinebretiére, J. Mercurio, and A. Dauger, "X-ray diffraction line broadening by stacking faults in $SrBi_2Nb_2O_9$/$SrTiO_3$ epitaxial thin films," *Thin Solid Films*, vol. 391, no. 1, pp. 42–46, 2001.
31. E. Eberg, Å. F. Monsen, T. Tybell, A. T. van Helvoort, and R. Holmestad, "Comparison of tem specimen preparation of perovskite thin films by tripod polishing and conventional ion milling," *J. Electron Microsc.*, vol. 57, no. 6, pp. 175–179, 2008.

32. M. Eriksson, J. Sainio, and J. Lahtinen, "Chromium deposition on ordered alumina films: An x-ray photoelectron spectroscopy study of the interaction with oxygen," *J. Chem. Phys.*, vol. 116, no. 9, pp. 3870–3874, 2002.

33. S. S. Li and Y. M. Hu, "Transition from weak ferromagnetism to strong paramagnetism in $Zn_{1-x}Cr_xO$ ($0 \leq x \leq 0.026$) thin films," *J. Phys. Conf. Ser.*, vol. 266, no. 1, p. 012018, 2011.

34. J. Sainio, M. Aronniemi, O. Pakarinen, K. Kauraala, S. Airaksinen, O. Krause, and J. Lahtinen, "An xps study of crox on a thin alumina film and in alumina supported catalysts," *Appl. Surf. Sci.*, vol. 252, no. 4, pp. 1076–1083, 2005.

35. M. C. Biesinger, C. Brown, J. R. Mycroft, R. D. Davidson, and N. S. McIntyre, "X-ray photoelectron spectroscopy studies of chromium compounds," *Surf. Interface Anal.*, vol. 36, no. 12, pp. 1550–1563, 2004.

36. M. Aronniemi, J. Sainio, and J. Lahtinen, "Chemical state quantification of iron and chromium oxides using xps: the effect of the background subtraction method," *Surf. Sci.*, vol. 578, no. 13, pp. 108–123, 2005.

37. E. Seim, "TEM characterization of Cr-doped ZnS thin films for solar cell applications," Master's thesis, Norwegian University of Science and Technology, 2014.

38. E. Spiecker, V. Radmilovic, and U. Dahmen, "Quantitative TEM analysis of 3-D grain structure in CVD-grown SiC films using double-wedge geometry," *Acta Materialia*, vol. 55, no. 10, pp. 3521 – 3530, 2007.